Letter

Continuously tunable topological defects and topological edge states in dielectric photonic crystals

Shiwei Tang,[1] Yikai Xu,[1] Fei Ding,[2] and Feng Liu[1,3,*]

[1]*School of Physical Science and Technology, Ningbo University, Ningbo 315-211, China*

[2]*SDU Nano Optics, University of Southern Denmark, Campusvej 55, DK-5230 Odense, Denmark*

[3]*Institute of High-Pressure Physics, Ningbo University, Ningbo 315-211, China*

(Received 15 August 2022; revised 17 November 2022; accepted 23 December 2022; published 17 January 2023)

Topological defects in solid-state materials are crystallographic imperfections that local perturbations cannot remove. Owing to their nontrivial real-space topology, topological defects such as dislocations and disclinations could trap anomalous states associated with nontrivial momentum-space topology. The real-space topology of dislocations and disclinations can be characterized by the Burgers vector **B**, which is usually a fixed fraction and integer of the lattice constant in solid-state materials. Here we show that in a dielectric photonic crystal—an artificial crystalline structure—it is possible to tune **B** continuously as a function of the dielectric constant of dislocations. Through this unprecedented tunability of **B**, we achieve proper controls of topological interfacial states, i.e., reversal of their helicities. Based on this fact, we propose a topological optical switch controlled by the dielectric constant of the tunable dislocation. Our results shed light on the interplay of real and reciprocal space topologies and offer a scheme to implement scalable and tunable robust topological waveguides in dielectric photonic crystals.

DOI: 10.1103/PhysRevB.107.L041403

Introduction. Topological photonic crystals are an emerging field that explores nontrivial topology in momentum space using artificial periodic arrangements of dielectrics and metals in the notation of electromagnetic (EM) waves [1–5]. Based on nontrivial edge states of topological photonic crystals, tremendous applications have been proposed and realized, such as the unidirectional waveguides [6–13], the EM cavities with ultrahigh-quality factors [14–16], and highly efficient single-mode lasers [17–19]. Distinct from their conventional counterparts, the nontrivial topology of momentum space renders these applications robust against defects in real space. The robustness of these EM states originates from the bulk-edge correspondence principle, which links the real-space profiles of EM waves to the nontrivial topology of photonic bulk band structure, lying at the heart of topological band theory [20–22].

Very recently, topological defects such as dislocation and disclination have drawn increasing attention because of their interplay with the momentum-space topology [23–28]. Due to their nontrivial real-space topology, topological defects could trap anomalous states around them, revealing the nontrivial momentum-space topology [29–34]. This remarkable fact extends the bulk-edge correspondence principle to the bulk-edge-defect one [35–38], which enables large-scale implementation of topological edge states [39]. Real-space topology of dislocations and disclinations is characterized by the Burgers vector **B**, which measures the magnitude and direction of lattice distortion induced by these topological defects [40]. In solid-state materials, **B** is fixed at values of several lattice constants a_0 because of the indivisibility of atoms. However, this is not the case in artificial crystalline structures like photonic crystals, where macroscopic dielectric units mimic atoms and can bring unrealized tunability of **B** together with novel topological physics.

In this work, we focus on a representative topological photonic crystal with Kekulé-like hopping textures [41]. By introducing an artificial dislocation line made of dielectric rods in the designed photonic crystal, topological edge states can be trapped around the line defect [42,43]. Through modifying the dielectric constant ε of rods in the dislocation, the dispersion of topological edge states can be continuously tuned according to the relation $v \sim \mathbf{P} \cdot \mathbf{B}$ with **P** being the vectored Zak phase and v being the topological index. Interestingly, unlike the cases of solid-state materials, where v is either zero or other integers, v becomes $v(\varepsilon)$ in the designed photonic crystal, a function of ε that can be continuously tailored in a precise manner. In a specific ε range, we find the helicity of topological edge states can be reversed, i.e., an opposite group velocity combined with the same spin polarization. Our results offer an unrealized tunability of topological defects in crystalline systems that yields new possibilities for engineering topological edge states together with potential applications, such as a topological optical switch controlled by the dielectric constant of the dislocation. The numerical simulations in this work are done using the finite-element method by COMSOL.

Topological photonic crystal. The designed photonic crystal is depicted in Fig. 1(a), where six rods of dielectric constant $\varepsilon_c = 11$ and radius r form a unit cell arranged on a hexagonal lattice of primitive vectors $\mathbf{a}_1$ and $\mathbf{a}_2$ of length a_0. The corresponding 1st Brillioun zone is displayed in Fig. 1(b), where $\mathbf{b}_1$ and $\mathbf{b}_2$ are the two primitive vectors of the momentum space. By fixing the distance of neighboring dielectric rods, i.e., R in

*Liufeng@nbu.edu.cn

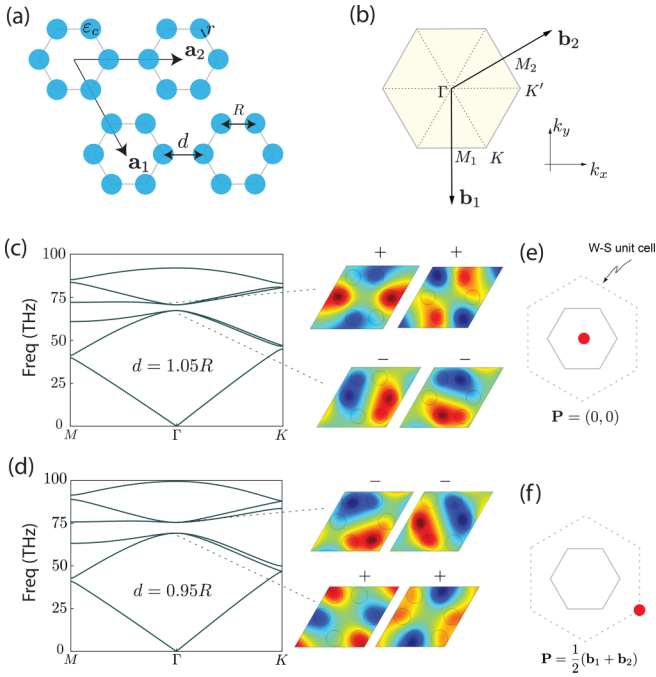

FIG. 1. (a) Schematic of the designed hexagonal photonic crystal. In a unit cell, six rods of dielectric constant ε_c and radius r sit on the vertices of the hexagon separated by a distance R within a unit cell and a distance d between unit cells. The primitive vectors of the designed photonic crystal are $\mathbf{a}_1 = a_0(\frac{1}{2}, -\frac{\sqrt{3}}{2})$ and $\mathbf{a}_2 = a_0(1, 0)$ with a_0 the lattice constant. In the numerical simulations, we take $r =$ 235 nm, $R = 705$ nm, and $\varepsilon_c = 11$. (b) Corresponding 1st Brillouin zone of the designed photonic crystal, where $\mathbf{b}_1 = \frac{2\pi}{a_0}(0, -\frac{2}{\sqrt{3}})$ and $\mathbf{b}_2 = \frac{2\pi}{a_0}(1, \frac{1}{\sqrt{3}})$. (c) and (d) Photonic band structures of the designed photonic crystal for $d = 1.05R$ and $d = 0.95R$, respectively. A band inversion happens at Γ between a pair of p_x, p_y EM modes and a pair of $d_{x^2-y^2}$, d_{xy} EM modes when $d = R$. "$\pm$" indicates the parity of EM modes. (e) and (f) Wannier centers of the designed photonic crystal for $d = 1.05R$ and $d = 0.95R$, respectively. The inner hexagon indicates the positions of six dielectric rods, the dashed outside hexagon indicates the Wigner-Seitz unit cell, and the red dot is the center of the Wannier function.

the same unit cell, the integral hopping among unit cells can be tuned by the distance d between two neighboring unit cells. In the case of $d = R$, when all the dielectric rods are equally separated, the designed photonic crystal becomes a photonic version of graphene and has a similar photonic band structure [44–48]. Because of the enlarged unit cell (six "atoms" in a unit cell) in the designed photonic crystal, Dirac cones that are located initially at the K and K' points in graphene are folded back to the Γ point here, as displayed in Figs. 1(c) and 1(d).

Similar to the two-dimensional Su-Schrieffer-Heeger model [49,50], the designed photonic crystal experiences a topological phase transition when d is tuned, which effectively alters the ratio of integral hoppings of those dielectric rods within the same unit-cell and between neighboring unit cells. For the nontrivial topological phase, where the neighboring unit cells have stronger couplings, i.e., $d < R$, topological edge and corner states appear in the designed photonic crystal. The appearance of these topological states is due to a band inversion happening at the Γ point between a pair of p_x, p_y modes and a pair of $d_{x^2-y^2}$, d_{xy} modes as displayed in Figs. 1(c) and 1(d), which leads to a shift of Wannier center of EM waves in those inverted photonic bands [51,52]. As displayed in Figs. 1(e) and 1(f), the Wannier center of the EM wave of an inverted band shifts from the middle of the unit cell for the trivial phase to the boundary of the unit cell for the nontrivial phase, which is directly related to a geometric phase—the vectored Zak phase determined by the symmetric properties of EM waves at high-symmetric $\mathbf{k}$ points as [53–55]

$$P_i^n = -\mathrm{i} \ln \frac{\eta^n(M_i)}{\eta^n(\Gamma)}, \tag{1}$$

where the subindex i indicates the component of $\mathbf{P}$ along $\mathbf{b}_i$ and $\eta^n(\mathbf{k})$ denotes the parity of the EM wave of the nth photonic band at point $\mathbf{k}$. Because of crystalline and inversion symmetries, P_i^n takes either 0 for the trivial phase or π for the nontrivial phase. Essentially, the topological phase of the designed photonic crystal is not a strong topological phase but an obstructed atomic phase, and it can host robust unidirectional edge states and corner states due to the band inversion protected by a sizable band gap [56–58]. The obstructed atomic phase can be characterized by the Wannier center, which is either $P_i^2 b_i/2\pi$ or $P_i^3 b_i/2\pi$ of the degenerate second and third bands in the designed photonic crystal. It is noted that the summation of P_i^n over the three bands below the band gap always vanishes due to the C_{6v} point group symmetry, which reflects the fragile topology of the designed photonic crystal [59–61]. By a perturbation that separates the first and second photonic bands, it is seen that the second and third bands have nontrivial Wilson loops while all three bands together have a trivial one [61]. Furthermore, as discussed later, a pair of pseudospins can be constructed by the degenerate second and third bands, which enables us to count P_i^2 and P_i^3 separately. In later discussions, we denote $\mathbf{P}$ as the Wannier center of the designed photonic crystal, which is $(\frac{P_1^2}{2\pi}, \frac{P_2^2}{2\pi})$ in terms of $\mathbf{b_1}$ and $\mathbf{b}_2$ effectively. For the nontrivial phase where topological edge states appear, we have $\mathbf{P} = \frac{1}{2}(\mathbf{b}_1 + \mathbf{b}_2)$, similar to the weak index of three-dimensional topological insulators [62]. Alternatively, the nest-Wilson loop can also be used for characterizing the obstructed atomic phase of the designed photonic crystal [63,64].

B(ε) *and helicity reversal.* Dislocations are topological line defects in crystalline systems which introduce discontinuity to the crystalline order characterized by **B**. To measure **B**, one may construct a circuit around the dislocation interface, and **B** is given by the extra path that cannot be canceled out in the circuit. In solid-state materials, by preserving the crystalline symmetry, the amplitude of **B** is always one or several units of the lattice for a complete dislocation and a fraction of the lattice for a partial one (i.e., inserting a line defect made by incomplete unit cells). Owing to the lattice distortion associated with the dislocation, a $U(1)$ gauge field $A_i = -\boldsymbol{\varepsilon_i} \cdot \mathbf{K}_{\mathrm{inv}}$ minimally couples to the excitations such as topological edge states, and a linear dispersion $\sim \mathbf{k} \cdot \mathbf{t}$ develops [30,36,65]. Here $\mathbf{K}_{\mathrm{inv}}$ is either the band inversion $\mathbf{k}$ point or its equivalence, like Γ and M in Eq. (1), and $\mathbf{t}$ is the directional vector of the dislocation line. This is the so-called **K-B-t** rule [36]. It is noted that we can apply the **K-B-t** rule to photonic crystals,

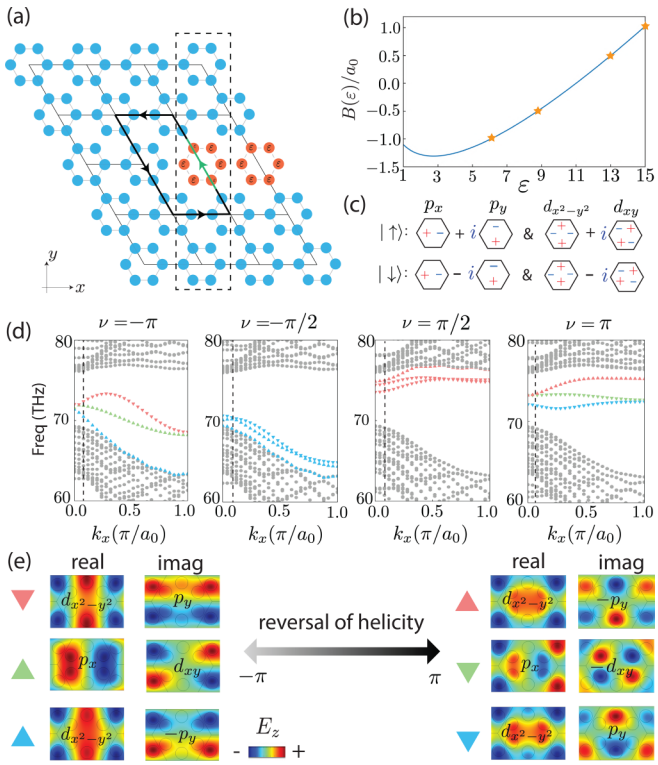

FIG. 2. (a) Schematic of the continuously tunable dislocation interface in the designed photonic crystal. The tunable dislocation comprises a semi-infinite line of defected units made of rods of radius $r' = r$ and dielectric constant ε. The green vector indicates the Burgers vector $\mathbf{B}$ of the tunable dislocation for $\varepsilon = 1$. The dashed rectangle is a schematic of the ribbon with periodic boundary conditions in both directions, which is used for the calculations of the photonic band structure with the tunable dislocation located at the middle, i.e., ribbon spectra in (c). (b) The magnitude of effective Burgers vector experienced by EM modes as a function of ε. Four stars are the positions for $B(\varepsilon)/a_0 = -1, -0.5, 0.5$, and 1, accordingly. (c) Possible combinations of pseudospins composed by doubly degenerate EM modes such as $p_x \pm ip_y$ and $d_{x^2-y^2} \pm id_{xy}$. (e) EM modes of edge states located at the tunable dislocations for $\nu = -\pi$ and $\nu = \pi$. (d) Ribbon spectra with the tunable dislocation located at the middle for different $\nu = B(\varepsilon)\pi/a_0$. The triangles are those edge states located at the tunable dislocation, whose directions represent the pseudospin polarization and their colors indicate the group velocities at $k_x = 0.04$ around Γ; i.e., red is positive, blue is negative, and green is almost zero.

as Maxwell's equations for two-dimensional photonic crystals could be reformulated in a tight-binding scheme with a Hamiltonian $\mathcal{H} = -\partial^2/\varepsilon(\mathbf{r})$ [50,65]. There are two essential differences between the photonic and electronic systems; one is the spin degree of freedom, and the other is the long-range interactions. For spins, it can be mimicked by the orbital momentum (photonic eigenmode) in the designed photonic crystal, as discussed later. For long-range interactions, it does not impact the topological properties of the designed photonic crystal [56].

Figure 2(a) displays a dislocation *interface* in the designed photonic crystal created by inserting a semi-infinite line of unit cells with a tunable dielectric constant ε, where a circuit around the dislocation interface is plotted, and a path along the defected site is marked by green. It is noted that we only consider a dislocation interface here rather than a complete dislocation because the nontrivial flux originates from the dislocation core only. Owing to the tunable ε, $\mathbf{B}$ becomes $\mathbf{B}(\varepsilon)$, i.e., $\mathbf{B} = 0$ if $\varepsilon = \varepsilon_c$ and $\mathbf{B} = -\mathbf{a}_1$ if $\varepsilon = 1$ [65]. For the nontrivial topological phase of the designed photonic crystal that $\mathbf{P} = \frac{1}{2}(\mathbf{b}_1 + \mathbf{b}_2)$, the introduced line defect traps the topological edge states based on the following relation,

$$\nu = \mathbf{P} \cdot \mathbf{B}, \tag{2}$$

where $\mathbf{P}$ plays a role similar to the weak index of 3D topological insulators [62]. Finite ν introduces an effective equivalent flux around the defect core according to the **K-B-t** rule [36,65]. In the designed photonic crystal, because the effective length of $\mathbf{B}$ is determined by the optical path difference rather than the actual real-space distance, the effective flux becomes $B(\varepsilon)\pi/a_0$, which is different from the values of either π or 0 in solid-state materials. As suggested by the green vector in Fig. 2(a), the effective optical path difference $B(\varepsilon)$ can be approximately written as

$$B(\varepsilon) = 4R\alpha(\sqrt{\varepsilon} - \sqrt{\varepsilon_c}), \tag{3}$$

where α is a coefficient determined by eigenfrequency and we set $\alpha = \sqrt{\varepsilon}$ here [66]. We plot $B(\varepsilon)$ in Fig. 2(b), and for validity we focus on the flux range where $B(\varepsilon) \in [-a_0, a_0]$. As displayed in Fig. 2(b), B varies continuously with ε and changes its sign at $\varepsilon = \varepsilon_c$ and $B \approx -a_0$ for $\varepsilon = 1$. Because of $B(\varepsilon)$ and the corresponding $\nu(\varepsilon)$, it is possible to tune the edge states trapped around the dislocation through ε, and the time-reversal pairs couple the distortion-induced gauge field oppositely. Thanks to the C_{6v} point group symmetry, two pairs of pseudospins can be constructed by linear combinations of degenerate EM modes, such as $p_x + ip_y$, $d_{x^2-y^2} + id_{xy}$ for spin-up and $p_x - ip_y$, $d_{x^2-y^2} - id_{xy}$ for spin-down as displayed in Fig. 2(c), where a general time-reversal operator $\mathcal{T} = KU$ can be constructed [41].

To demonstrate the tunability of dislocation-bound states by ε, we calculate ribbon spectra for several typical values of ε where the tunable dislocation is located at the middle of the ribbon with the Floquet periodic boundary condition along the x direction and periodic boundary condition along the y direction as indicated by the dashed rectangle in Fig. 2(a). This setup is similar to tiling the periodic layers of an edge dislocation along the z direction ($\mathbf{t} = \hat{\mathbf{z}}$) on the xy plane over the x direction, which enables us to check the spectrum of dislocation-bound states [65]. As displayed in Fig. 2(c), the ribbon spectra are calculated and plotted for $\varepsilon = 6.125, 8.77, 13$, and 15 [marked by stars in Fig. 2(b)], which correspond to fluxes $-\pi, -\pi/2, \pi/2$, and π, respectively. From Fig. 2(c), we see three edge states in the photonic band gap, and linear dispersions arise around the Γ point for $\nu = \pm\pi$, consistent with the prediction of the **K-B-t** rule. Their spin polarization is marked as triangles, and different colors represent their group velocities around the Γ point, as there are two types of representations for the pseudo-spin-up and -down, which suggests that actual pseudospin polarization of topological edge states could be any linear combination of these two representations. Also, we observe three edge states rather than two or four because of the specific ε range we

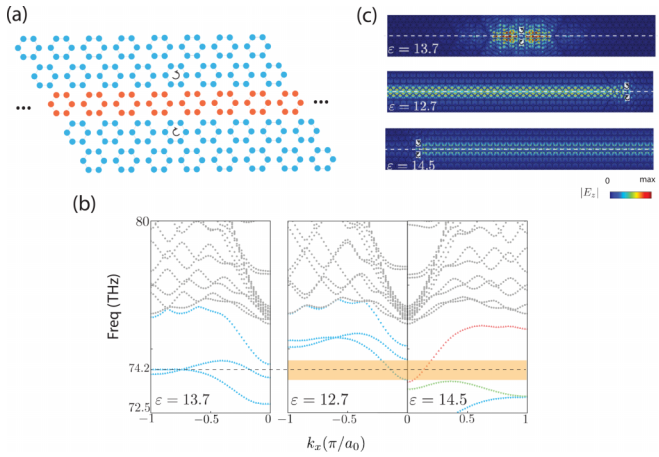

FIG. 3. (a) Schematic of the proposed topological optical switch made by the tunable dislocation in the designed photonic crystal. The red/blue are the defective/standard units. The left and right rotating arrows indicate two sets of four-point sources with different phases at each point such as $(0, \pi/2, \pi, 3\pi/2)$ and $(0, -\pi/2, -\pi, -3\pi/2)$ in anticlockwise order. (b) Combined ribbon spectra for the tunable dislocation of $\varepsilon = 12.7$, 13.7, and 14.5. In a range around 74.2 THz, as marked by a yellow square, the left-going and right-going edge states have the same pseudospin polarization, where we can control the propagation of edge states by tuning the dislocation's dielectric constant. Furthermore, for $\varepsilon = 13.7$, the edge state becomes localized because of the crossover of two edge states at 74.2 THz. (c) Propagation and localization of edge states excited by the rotating sources in the tunable dislocation for $\varepsilon = 13.7$, 12.7, and 14.5 at 74.2 THz, accordingly. Dashed lines indicate positions of the tunable dislocation.

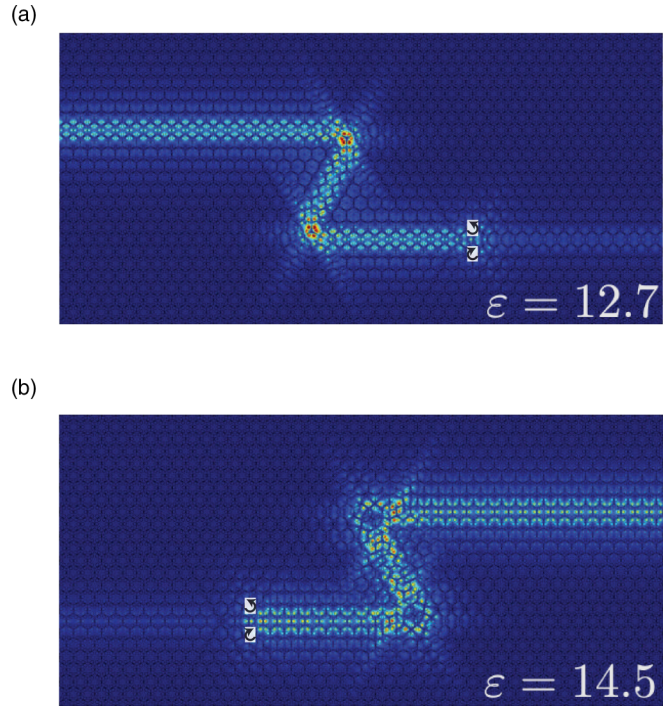

FIG. 4. Demonstration of topological protection of the excited edge states at the tunable dislocation for (a) $\varepsilon = 12.7$ and (b) $\varepsilon = 14.5$.

focus on. From Fig. 2(c), we observe two effects of changing effective flux ν. The first effect is a continuous modification of the dispersion of topological edge states. As seen in Fig. 2(c), when ν changes from $-\pi$ to π, the dispersion of topological edge states changes accordingly. From $\nu = -\pi$ to 0, topological edge states are gradually pushed back to the bottom bulk states, and they reappear from the top bulk states with a contrasting dispersion for $\nu > 0$. Furthermore, when $\nu = \pm\pi$, the pseudo-spin-up and pseudo-spin-down edge states degenerate at the Γ point, while they are separated for $\nu = \pm\pi/2$, and for $\nu = \pm\pi$, the pseudo-spin-up and pseudo-spin-down edge states have different group velocities around the Γ point, while alike group velocity for $\nu = \pm\pi/2$. The second effect of changing ν is the reversal of the helicity of topological edge states. This is because of opposite effective magnetic fields for $\pm\nu$. As displayed in Figs. 2(c) and 2(e), for the edge states of the same pseudospin polarization, they have opposite group velocities; i.e., $d_{x^2-y^2} + ip_y$ has a positive group velocity at $k_x = 0.04$ for $\nu = -\pi$ and has a negative group velocity for $\nu = \pi$. It is noted that the similar tunability of dislocation-bound states can be arrived at by changing the rod radius of the defect sites as suggested by the **K-B-t** rule [65]. Furthermore, impedance plays an essential role in the formation of interface states, and we check these effects by a ribbon structure with an interface between the designed photonic crystal and the periodic defected sites for $d > R$ and $d < R$, respectively [65,67].

A topological optical switch. This unprecedented tunability of topological edge states brought by $B(\varepsilon)$ can be used for composing a topological optical switch controlled by ε. As displayed in Fig. 3(a), the topological optical switch is composed of a sandwich-like structure. The tunable dislocation is located at the middle layer of the designed photonic crystal. Two rotating sources for exciting spin-polarized edge states are located at the two sides of the dislocation. Figure 3(b) displays the combined ribbon spectra for $\varepsilon = 12.7$, 13.7, and 14.5. As displayed in Fig. 3(b) around a range 73–75 THz, there is an operating window where the pseudo-spin-up edge state is going left for $\varepsilon = 12.7$ and while it is going right for $\varepsilon = 14.5$. Furthermore, for $\varepsilon = 13.7$, two edge states intersect at 74.2 THz, leading to EM waves' localization. Making use of this operating window and the intersection of edge states, we can achieve an optical switch controlled by ε using a unified source at 74.2 THz, i.e., the EM wave going left, localizing, and going right for $\varepsilon = 12.7$, $\varepsilon = 13.7$, and $\varepsilon = 14.5$, respectively. As displayed in Fig. 3(c), the propagation of the topological edge states is wholly reversed when tuning ε from 12.7 to 14.5 and stops at $\varepsilon = 13.7$. The adjustment of ε can be realized by employing functional materials triggered by various external conditions such as applied voltage [68], light irradiation [69,70], temperature [71], and even applied magnetic field [72]. Compared with a conventional optical switch, the EM wave propagation in the designed photonic crystal is topologically protected and thus immune to real-space defects. As displayed in Fig. 4, the excited topological EM wave can pass through the "Z" turn without obvious backscattering, demonstrating their nontrivial topological nature. Furthermore, as the introduced line defects are

scalable, unlike the interfacial topological edges that require at least two topologically distinct bulk samples, the proposed topological optical switch can be implemented at a large scale, forming a topological optical switch network. Besides the topological optical switch, the structure in Fig. 3(a) also offers a detector for external parameter Q with a sensitivity determined by $Q(\varepsilon)$. For the experimental demonstration, the designed photonic crystal can be constructed with GaAs while the tunable dislocation material can use the phase-change materials [73,74].

Conclusion. We have introduced a continuously tunable topological defect in a photonic crystal consisting of dislocations with dynamically controlled dielectric constants, where the dispersion of topological edge states and their helicities can be tuned and reversed. The tunability of topological edge states in the designed photonic crystal is attributed to the interplay between real-space and momentum-space topologies, where an effective flux $\mathbf{P} \cdot \mathbf{B}/a_0$ arises. Based on the tunable topological defect in the designed photonic crystal, we have proposed a topologically robust and scalable optical switch, which various external conditions can control.

Acknowledgments. This work is supported by the Research Starting Funding of Ningbo University, NSFC Grant No. 12074205, and NSFZP Grant No. LQ21A040004. S.-W.T. is supported by the National Natural Science Foundation of China (Grant No. 11604167) and Natural Science Foundation of Ningbo (Grant No. 2021J073). F.D. is supported by Danmarks Frie Forskningsfond (Grant No. 1134-00010B) and Villum Fonden (Grant No. 37372). F.L. appreciates beneficial discussions with F. Nori.

[1] L. Lu, J. Joannopoulos, and M. Soljai, Topological photonics, Nat. Photonics **8**, 821 (2014).
[2] T. Ozawa, H. M. Price, A. Amo, N. Goldman, M. Hafezi, L. Lu, M. C. Rechtsman, D. Schuster, J. Simon, O. Zilberberg, and I. Carusotto, Topological photonics, Rev. Mod. Phys. **91**, 015006 (2019).
[3] M. Rider, S. Palmer, S. Pocock, X. Xiao, P. Arroyo Huidobro, and V. Giannini, A perspective on topological nanophotonics: Current status and future challenges, J. Appl. Phys. **125**, 120901 (2019).
[4] H. Wang, S. K. Gupta, B.-Y. Xie, and M.-H. Lu, Topological photonic crystals: A review, Front. Optoelectron. **13**, 50 (2020).
[5] B. Xie, H.-X. Wang, X. Zhang, P. Zhan, J.-H. Jiang, M. Lu, and Y. Chen, Higher-order band topology, Nat. Rev. Phys. **3**, 520 (2021).
[6] F. D. M. Haldane and S. Raghu, Possible Realization of Directional Optical Waveguides in Photonic Crystals with Broken Time-Reversal Symmetry, Phys. Rev. Lett. **100**, 013904 (2008).
[7] Z. Wang, Y. Chong, J. Joannopoulos, and M. Soljai, Observation of unidirectional backscattering-immune topological electromagnetic states, Nature (London) **461**, 772 (2009).
[8] A. Khanikaev, S. Hossein Mousavi, W.-K. Tse, M. Kargarian, A. Macdonald, and G. Shvets, Photonic topological insulators, Nat. Mater. **12**, 233 (2013).
[9] F. Deng, Y. Sun, X. Wang, R. Xue, Y. Li, H. Jiang, Y. Shi, K. Chang, and H. Chen, Observation of valley-dependent beams in photonic graphene, Opt. Express **22**, 23605 (2014).
[10] D. Leykam, K. Y. Bliokh, C. Huang, Y. D. Chong, and F. Nori, Edge Modes, Degeneracies, and Topological Numbers in Non-Hermitian Systems, Phys. Rev. Lett. **118**, 040401 (2017).
[11] C. Li, X. Hu, H. Yang, and Q. Gong, Unidirectional transmission in 1D nonlinear photonic crystal based on topological phase reversal by optical nonlinearity, AIP Adv. **7**, 025203 (2017).
[12] Y. Yang, Y. F. Xu, T. Xu, H.-X. Wang, J.-H. Jiang, X. Hu, and Z. H. Hang, Visualization of a Unidirectional Electromagnetic Waveguide Using Topological Photonic Crystals Made of Dielectric Materials, Phys. Rev. Lett. **120**, 217401 (2018).
[13] Q. Chen, L. Zhang, F. Chen, Q. Yan, R. Xi, H. Chen, and Y. Yang, Photonic topological valley-locked waveguides, ACS Photonics **8**, 1400 (2021).
[14] Y. Ota, F. Liu, R. Katsumi, K. Watanabe, K. Wakabayashi, Y. Arakawa, and S. Iwamoto, Photonic crystal nanocavity based on a topological corner state, Optica **6**, 786 (2019).
[15] B.-Y. Xie, G.-X. Su, H.-F. Wang, H. Su, X.-P. Shen, P. Zhan, M.-H. Lu, Z.-L. Wang, and Y.-F. Chen, Visualization of Higher-Order Topological Insulating Phases in Two-Dimensional Dielectric Photonic Crystals, Phys. Rev. Lett. **122**, 233903 (2019).
[16] S. Iwamoto, Y. Ota, and Y. Arakawa, Recent progress in topological waveguides and nanocavities in a semiconductor photonic crystal platform [invited], Opt. Mater. Express **11**, 319 (2021).
[17] G. Harari, M. A. Bandres, Y. Lumer, M. C. Rechtsman, Y. D. Chong, M. Khajavikhan, D. N. Christodoulides, and M. Segev, Topological insulator laser: Theory, Science **359**, eaar4003 (2018).
[18] H. Zhao, P. Miao, M. Teimourpour, S. Malzard, R. El-Ganainy, H. Schomerus, and L. Feng, Topological hybrid silicon microlasers, Nat. Commun. **9**, 981 (2018).
[19] Y. Ota, R. Katsumi, K. Watanabe, S. Iwamoto, and Y. Arakawa, Topological photonic crystal nanocavity laser, Commun. Phys. **1**, 86 (2018).
[20] Y. Hatsugai, Chern Number and Edge States in the Integer Quantum Hall Effect, Phys. Rev. Lett. **71**, 3697 (1993).
[21] L. Fu and C. L. Kane, Time reversal polarization and a Z_2 adiabatic spin pump, Phys. Rev. B **74**, 195312 (2006).
[22] Y. Hwang, J. Ahn, and B.-J. Yang, Fragile topology protected by inversion symmetry: Diagnosis, bulk-boundary correspondence, and Wilson loop, Phys. Rev. B **100**, 205126 (2019).
[23] F.-F. Li, H.-X. Wang, Z. Xiong, Q. Lou, P. Chen, R.-X. Wu, Y. Poo, J.-H. Jiang, and S. John, Topological light-trapping on a dislocation, Nat. Commun. **9**, 2462 (2018).
[24] Y. Liu, S. Leung, F.-F. Li, Z.-K. Lin, X. Tao, Y. Poo, and J.-H. Jiang, Bulk-disclination correspondence in topological crystalline insulators, Nature (London) **589**, 381 (2021).
[25] H. Xue, D. Jia, Y. Ge, Y.-j. Guan, Q. Wang, S.-q. Yuan, H.-x. Sun, Y. D. Chong, and B. Zhang, Observation of Dislocation-Induced Topological Modes in a Three-Dimensional Acoustic Topological Insulator, Phys. Rev. Lett. **127**, 214301 (2021).
[26] Y. Deng, W. A. Benalcazar, Z.-G. Chen, M. Oudich, G. Ma, and Y. Jing, Observation of Degenerate Zero-Energy Topological

States at Disclinations in an Acoustic Lattice, Phys. Rev. Lett. **128**, 174301 (2022).
[27] S. Yamada, T. Li, M. Lin, C. Peterson, T. Hughes, and G. Bahl, Bound states at partial dislocation defects in multipole higher-order topological insulators, Nat. Commun. **13**, 2035 (2022).
[28] L. Ye, C. Qiu, M. Xiao, T. Li, J. Du, M. Ke, and Z. Liu, Topological dislocation modes in three-dimensional acoustic topological insulators, Nat. Commun. **13**, 508 (2022).
[29] L. Fu, Topological Crystalline Insulators, Phys. Rev. Lett. **106**, 106802 (2011).
[30] R.-J. Slager, A. Mesaros, V. Jurii, and J. Zaanen, The space group classification of topological band-insulators, Nat. Phys. **9**, 98 (2013).
[31] M. Vergniory, L. Elcoro, C. Felser, N. Regnault, B. Bernevig, and Z. Wang, A complete catalogue of high-quality topological materials, Nature (London) **566**, 480 (2019).
[32] T. Zhang, Y. Jiang, Z. Song, H. Huang, Y. He, Z. Fang, H. Weng, and C. Fang, Catalogue of topological electronic materials, Nature (London) **566**, 475 (2019).
[33] F. Tang, H. Po, A. Vishwanath, and X. Wan, Comprehensive search for topological materials using symmetry indicators, Nature (London) **566**, 486 (2019).
[34] B. Roy and V. Juričić, Dislocation as a bulk probe of higher-order topological insulators, Phys. Rev. Res. **3**, 033107 (2021).
[35] Y. Ran, Y. Zhang, and A. Vishwanath, One-dimensional topologically protected modes in topological insulators with lattice dislocations, Nat. Phys. **5**, 298 (2009).
[36] R.-J. Slager, A. Mesaros, V. Juričić, and J. Zaanen, Interplay between electronic topology and crystal symmetry: Dislocation-line modes in topological band insulators, Phys. Rev. B **90**, 241403(R) (2014).
[37] J. C. Teo and T. L. Hughes, Topological defects in symmetry-protected topological phases, Annu. Rev. Condens. Matter Phys. **8**, 211 (2017).
[38] M. Geier, I. C. Fulga, and A. Lau, Bulk-boundary-defect correspondence at disclinations in rotation-symmetric topological insulators and superconductors, SciPost Phys. **10**, 092 (2021).
[39] Q. Wang, H. Xue, B. Zhang, and Y. D. Chong, Observation of Protected Photonic Edge States Induced by Real-Space Topological Lattice Defects, Phys. Rev. Lett. **124**, 243602 (2020).
[40] M. Kleman and J. Friedel, Disclinations, dislocations, and continuous defects: A reappraisal, Rev. Mod. Phys. **80**, 61 (2008).
[41] L.-H. Wu and X. Hu, Scheme for Achieving a Topological Photonic Crystal by Using Dielectric Material, Phys. Rev. Lett. **114**, 223901 (2015).
[42] Z. Jiang, Y. Gao, L. He, H. Song, J. Zhou, and R. Zhu, Helical edge states of topological photonic crystals with line defects, Appl. Opt. **58**, 2294 (2019).
[43] M. Chen, L. Jiang, Z. Lan, and W. Sha, Pseudospin-polarized topological line defects in dielectric photonic crystals, IEEE Trans. Antennas Propag. **68**, 609 (2020).
[44] M. C. Rechtsman, Y. Plotnik, J. M. Zeuner, D. Song, Z. Chen, A. Szameit, and M. Segev, Topological Creation and Destruction of Edge States in Photonic Graphene, Phys. Rev. Lett. **111**, 103901 (2013).
[45] M. Bellec, U. Kuhl, G. Montambaux, and F. Mortessagne, Manipulation of edge states in microwave artificial graphene, New J. Phys. **16**, 113023 (2014).
[46] K. Y. Bliokh, D. Smirnova, and F. Nori, Quantum spin Hall effect of light, Science **348**, 1448 (2015).
[47] D. Song, V. Paltoglou, S. Liu, Y. Zhu, D. Gallardo, L. Tang, J. Xu, M. Ablowitz, N. Efremidis, and Z. Chen, Unveiling pseudospin and angular momentum in photonic graphene, Nat. Commun. **6**, 6272 (2015).
[48] G. Montambaux, Artificial graphenes: Dirac matter beyond condensed matter, C. R. Phys. **19**, 285 (2018).
[49] F. Liu and K. Wakabayashi, Novel Topological Phase with a Zero Berry Curvature, Phys. Rev. Lett. **118**, 076803 (2017).
[50] F. Liu, H.-Y. Deng, and K. Wakabayashi, Topological photonic crystals with zero Berry curvature, Phys. Rev. B **97**, 035442 (2018).
[51] R. D. King-Smith and D. Vanderbilt, Theory of polarization of crystalline solids, Phys. Rev. B **47**, 1651 (1993).
[52] R. Resta, Manifestations of Berry's phase in molecules and condensed matter, J. Phys.: Condens. Matter **12**, R107 (2000).
[53] C. Fang, M. J. Gilbert, and B. A. Bernevig, Bulk topological invariants in noninteracting point group symmetric insulators, Phys. Rev. B **86**, 115112 (2012).
[54] F. Liu, M. Yamamoto, and K. Wakabayashi, Topological edge states of honeycomb lattices with zero Berry curvature, J. Phys. Soc. Jpn. **86**, 123707 (2017).
[55] W. A. Benalcazar, T. Li, and T. L. Hughes, Quantization of fractional corner charge in C_n-symmetric higher-order topological crystalline insulators, Phys. Rev. B **99**, 245151 (2019).
[56] M. Proctor, P. A. Huidobro, B. Bradlyn, M. B. de Paz, M. G. Vergniory, D. Bercioux, and A. García-Etxarri, Robustness of topological corner modes in photonic crystals, Phys. Rev. Res. **2**, 042038(R) (2020).
[57] F. Liu and K. Wakabayashi, Higher-order topology and fractional charge in monolayer graphene, Phys. Rev. Res. **3**, 023121 (2021).
[58] H. T. Phan, F. Liu, and K. Wakabayashi, Valley-dependent corner states in honeycomb photonic crystals without inversion symmetry, Opt. Express **29**, 18277 (2021).
[59] F. Liu, H.-Y. Deng, and K. Wakabayashi, Helical Topological Edge States in a Quadrupole Phase, Phys. Rev. Lett. **122**, 086804 (2019).
[60] H. C. Po, H. Watanabe, and A. Vishwanath, Fragile Topology and Wannier Obstructions, Phys. Rev. Lett. **121**, 126402 (2018).
[61] M. B. de Paz, M. G. Vergniory, D. Bercioux, A. García-Etxarri, and B. Bradlyn, Engineering fragile topology in photonic crystals: Topological quantum chemistry of light, Phys. Rev. Res. **1**, 032005(R) (2019).
[62] F. Schindler, S. S. Tsirkin, T. Neupert, B. Andrei Bernevig, and B. J. Wieder, Topological zero-dimensional defect and flux states in three-dimensional insulators, Nat. Commun. **13**, 5791 (2022).
[63] B. Bradlyn, Z. Wang, J. Cano, and B. A. Bernevig, Disconnected elementary band representations, fragile topology, and Wilson loops as topological indices: An example on the triangular lattice, Phys. Rev. B **99**, 045140 (2019).
[64] S. J. Palmer, Revealing hidden topologies in photonic crystals, Ph.D. thesis, Imperial College London, 2021.
[65] See Supplemental Material at http://link.aps.org/supplemental/10.1103/PhysRevB.107.L041403 for details where the derivation of the tight-binding scheme of photonic crystals, the application of the $\mathbf{k}-\mathbf{B}-\mathbf{t}$ rule to two-dimensional dielectric photonic crystals, and the effects of changing rod radius and impedance are discussed.
[66] M. Hammer and O. Ivanova, Effective index approximations of

photonic crystal slabs: A 2-to-1-D assessment, Opt. Quantum Electron. **41**, 267 (2009).

[67] M. Xiao, Z. Q. Zhang, and C. T. Chan, Surface Impedance and Bulk Band Geometric Phases in One-Dimensional Systems, Phys. Rev. X **4**, 021017 (2014).

[68] D. E. Yıldız and İ Dökme, Frequency and gate voltage effects on the dielectric properties and electrical conductivity of $Al/SiO_2/p$-Si metal-insulator-semiconductor Schottky diodes, J. Appl. Phys. **110**, 014507 (2011).

[69] H. Zheng, E. Ryan, Y. Nishi, and J. Shohet, Effect of vacuum-ultraviolet irradiation on the dielectric constant of low-k organosilicate dielectrics, Appl. Phys. Lett. **105**, 202902 (2014).

[70] M. Veena, A. Somashekarappa, G. Shankaramurthy, H. Jayanna, and H. Somashekarappa, Effect of ^{60}Co gamma irradiation on dielectric and complex impedance properties of Dy^{3+} substituted Ni-Zn nanoferrites, J. Magn. Magn. Mater. **419**, 375 (2016).

[71] G. A. Samara, Temperature and pressure dependences of the dielectric constants of semiconductors, Phys. Rev. B **27**, 3494 (1983).

[72] T. Katsufuji and H. Takagi, Coupling between magnetism and dielectric properties in quantum paraelectric $EuTiO_3$, Phys. Rev. B **64**, 054415 (2001).

[73] Y. Zhang, J. Chou, J. Li, H. Li, Q. Du, A. Yadav, S. Zhou, M. Shalaginov, Z. Fang, H. Zhong, C. Roberts, P. Robinson, B. Bohlin, C. Ríos, H. Lin, M. Kang, T. Gu, J. Warner, V. Liberman, K. Richardson *et al.*, Broadband transparent optical phase change materials for high-performance nonvolatile photonics, Nat. Commun. **10**, 4279 (2019).

[74] M. Delaney, I. Zeimpekis, D. Lawson, D. Hewak, and O. Muskens, A new family of ultralow loss reversible phase-change materials for photonic integrated circuits: Sb_2S_3 and Sb_2Se_3, Adv. Funct. Mater. **30**, 2002447 (2020).